



Two-dimensional germanium monochalcogenides for photocatalytic water splitting with high carrier mobility



Xingshuai Lv, Wei Wei*, Qilong Sun, Fengping Li, Baibiao Huang, Ying Dai*

School of Physics, State Key Laboratory of Crystal Materials, Shandong University, 250100 Jinan, PR China

ARTICLE INFO

Article history:

Received 26 April 2017

Received in revised form 27 May 2017

Accepted 30 May 2017

Available online 3 June 2017

Keywords:

Two-dimensional GeX

Photocatalyst

Carrier mobility

Carrier separation

ABSTRACT

Highly efficient utilization of solar energy to split water into hydrogen and oxygen is regarded as a promising strategy to deal with the future energy crisis and environmental problems. To explore highly efficient and low-cost photocatalysts is highly desired. Herein, phosphorene-like germanium monochalcogenides (GeS and GeSe monolayers) are proposed here as efficient photocatalysts for water splitting. After confirming their stabilities, we observe that GeS exhibits an indirect band gap of 2.29 eV while GeSe reveals a direct band gap of 1.59 eV by HSE hybrid functional. Remarkably, high and directionally anisotropic carrier mobilities ($2430.50 \text{ cm}^2 \text{ V}^{-1} \text{ s}^{-1}$ for GeS and $4032.64 \text{ cm}^2 \text{ V}^{-1} \text{ s}^{-1}$ for GeSe) are quantitatively investigated by using deformation potential theory. In addition, GeS and GeSe monolayers exhibit a good separation of electrons and holes, which effectively reduces the photocatalytic activity with high efficiency. Upon the application of strain, the band structure can be modulated from semiconductor to metal and a direct-indirect bandgap transition is observed. Most intriguingly, the band gaps and band edge alignments at certain pH value can be effectively tuned to meet the requirement of the redox potential in water splitting. Finally, the adsorption and decomposition of water molecules on the surface of 2D GeS and the subsequent formation of hydrogen were explored, which unravels the mechanism of photocatalytic hydrogen production on 2D GeS. Our findings will be valuable for facilitating the exploration and application of GeS and GeSe for photocatalytic water splitting.

© 2017 Elsevier B.V. All rights reserved.

1. Introduction

As a promising form of clean energy, hydrogen is an ideal candidate for the replacement of fossil fuels in the future due to its high specific enthalpy of combustion and recycling possibility, with water as the only reaction product [1–3]. From the sustainable chemical point of view, sunlight-driven photocatalytic water splitting into renewable hydrogen fuel over the semiconductor photocatalysts has been regarded as a promising and efficient strategy to address current energy and environmental problems [4–6]. The water splitting process is that photocatalyst adsorbs solar light, generating electron-hole pairs. Subsequently, the water molecules are reduced by electrons to form H_2 and oxidized by holes to form O_2 . The key issue of this process is to develop novel photocatalysts with enhanced visible-light photocatalytic performance.

A desirable photocatalyst applicable to photocatalytic water splitting under visible light irradiation should not only be able to efficiently adsorb visible lights but also be nontoxic and earth-

abundant [7,8]. In recent years, water splitting draws a renewed interest due to the increasing challenges of energy and environmental problem and more efficient photocatalysts for water splitting sprung up both in experiments and in theories. Due to the large band gap of TiO_2 ($>3.0 \text{ eV}$) with low visible-light adsorption, there are various strategies to improve their photocatalytic performance, such as doping [9,10] and surface modification [11]. In addition, cocatalysts and dye sensitization are also efficient and widely used route to enhance the catalytic performance [12–14]. Following the pioneering study of UV-light-responsive TiO_2 photocatalyst [15], to date various visible-light-driven photocatalysts have been explored, including metal-organic frameworks (MOFs) and C_3N_4 -agar hybrid 3D material [16–18].

Beyond graphene [19], two-dimensional (2D) materials have been extensively investigated owing to their distinguished electronic, optical and mechanical properties [20–22]. It has been identified that 2D materials could be promising photocatalyst in view of the short distance for the generated electrons and holes to migrate, reducing the possibility of electron-hole recombination and giving rise to high quantum yield [23,24]. High specific surface area is also beneficial for the process of redox reaction to enhance the photocatalytic performance. For example, Xie et al.

* Corresponding authors.

E-mail addresses: weiw@sdu.edu.cn (W. Wei), daiy60@sdu.edu.cn (Y. Dai).

[25] experimentally reported that the single layer ZnSe exhibits enhanced photo-conversion efficiency with a photocurrent density up to 2.14 mA cm^{-2} , which is 195 times higher than that of its bulk phase. In addition, without using any noble metal cocatalyst, the photocatalytic hydrogen evolution rate under visible light of metal-free elemental black phosphorus (BP) nanosheets reaches $512 \mu\text{mol h}^{-1} \text{ g}^{-1}$, which is 18 times higher than that of the bulk BP, and is comparable or even higher than that of graphitic carbon nitrides ($\text{g-C}_3\text{N}_4$) [26].

Recently, group-IV monochalcogenides monolayers have emerged as a new class of 2D materials and attracted considerable attention due to advantages in high stability, earth abundant and environmental friendliness [27–30]. In a recent experiment, for example, GeX ($X=\text{S}, \text{Se}$) nanosheets have been successfully synthesized through a facile solution based approach, exhibiting a high photoresponsivity of up to 173 and 870 A W^{-1} under a 405 nm laser diode, respectively [31]. Previous study has uncovered that GeX monolayers possess wider band gaps than those of the bulk counterparts, suggesting that single-layer and double-layer SnSe and GeSe monolayers are promising materials for photovoltaic applications [32]. In addition, intriguing properties such as high surface area, auxetic mechanical feature, tunable electronic structure, excellent capability of harvesting sunlight and high carrier mobility are also presented in GeX monolayers [32,33]. In light of the desirable band structure and high carrier mobility, GeX monolayers therefore provide a novel platform for applications in photocatalytic water splitting. Considering that seeking for proper sunlight-driven photocatalysts for water splitting is one of the glorious missions of material science, we expect to give useful physical insights for 2D GeS and GeSe monolayers as photocatalysts in visible light water splitting, which has not been addressed in previous works up to now.

Herein, for the first time, we comprehensively investigate the structural and electronic properties of 2D GeS and GeSe monolayers, and profoundly discuss the separation and migration of photo-generated electrons/holes and redox capabilities. We find that GeS exhibits an indirect band gap while GeSe monolayer is a direct semiconductor, with the band gaps within visible light frequency. Remarkably, GeX monolayers exhibit high carrier mobility, indicating that the transfer of carriers to surface would be fast in the photocatalytic process. In view of the estimated low exciton binding energy, GeS and GeSe monolayers also exhibit high photo-generated carrier separation efficiency, which is beneficial for the

improvement of the photocatalytic activity. Furthermore, we reveal that the band gaps and band edge alignments could be effectively modified upon the exertion of biaxial strains to meet the requirement for redox potentials. The related properties all demonstrate that GeX monolayers have a great possibility to be considered as efficient photocatalysts for water splitting with tunable band structure and effective electron-hole separation.

2. Computational method

The first-principles calculations were carried out on the basis of density functional theory (DFT) as implemented in the Vienna *ab initio* simulation package (VASP) [34,35]. The ion-electron interactions were described using the projector-augmented-wave (PAW) approach [36]. For the exchange-correlation functional, the generalized gradient approximation (GGA) of Perdew-Burke-Ernzerhof (PBE) [37,38] was employed. The cutoff energy was set to be 450 eV, which is accurate enough to describe the outer valence electrons of $\text{Ge } 4s^24p^2$, $\text{S } 3s^23p^2$ and $\text{Se } 4s^24p^2$. The convergence criteria of energy and force were set to 10^{-5} eV/atom and $0.02 \text{ eV}/\text{\AA}$, respectively. In the geometry optimization and static self-consistent calculations, the k -point meshes of $11 \times 11 \times 1$ and $15 \times 15 \times 1$ generated by the Monkhorst-Pack Scheme [39] were used. $2 \times 2 \times 1$ supercells for GeS and GeSe monolayers are used in the calculations and we adopted a vacuum space of 20 \AA along z direction to avoid interactions between periodic images. The DFT-D2 semiempirical dispersion-correction approach was employed to correct the van der Waals (vdW) interactions [40]. In addition, compared to the underestimated band gaps with PBE functional [41], Heyd-Scuseria-Ernzerhof (HSE06) [42] hybrid functional was employed to better describe the electronic and optical properties [43]. Furthermore, *Ab initio* molecular dynamics (AIMD) calculations were carried out to examine the thermal stability of GeX monolayers, and 4×4 supercells at 500 K within each time step of 1 fs was considered.

3. Results and discussion

3.1. Structural and thermal stabilities of GeX monolayers

The relaxed structures of 2D GeX monolayers are shown in Fig. 1. GeX monolayers belong to the space group of $\text{Pm}\bar{1}21$ (No.

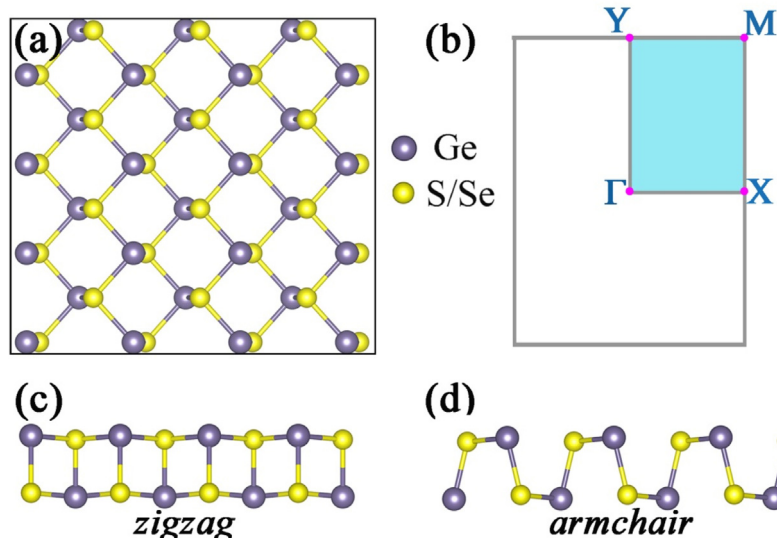


Fig. 1. (a) Top view of the atomic structure of GeX monolayers. (b) Brillouin zone of GeX monolayers. Side views of the atomic structure of GeX monolayers along (c) zigzag and (d) armchair directions.

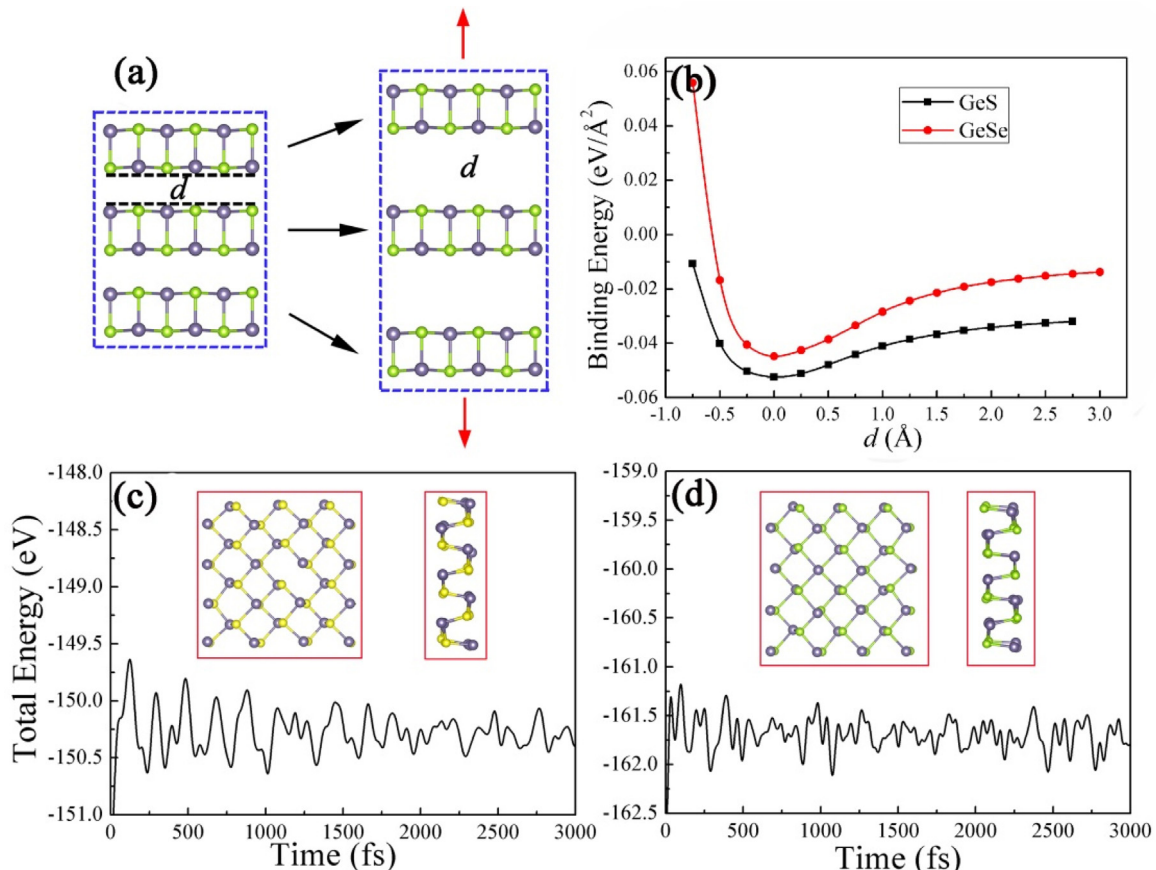


Fig. 2. (a) Models used for calculating the interlayer binding energy by changing the interlayer distance d . (b) Variation of the binding energy as a function of interlayer distance d . Here, we employ the interlayer distance $d = 3.14 \text{ \AA}$ of equilibrium structure as the reference. Total energy fluctuations during AIMD simulations of 2D (c) GeS and (d) GeSe at 500 K. The insets show snapshots of the structures after 3 ps from the 4×4 supercell.

$31 C_{2v}^7$) and exhibit a lattice structure analogue to phosphorene, exhibiting a puckered atomic layer with the sp^3 hybridization. Each Ge (S/Se) atom binds to two adjacent S/Se (Ge) atoms in the same atomic layer and one S/Se (Ge) atom in the next neighboring atomic layer. The lattice constants a and b of the fully optimized GeS (GeSe) monolayer is explored to be 4.39 and 3.67 \AA (4.30 and 3.92 \AA), respectively, and the average bond length between Ge and S (Se) atoms is estimated to be 2.44 \AA (2.59 \AA), which are in good agreement with previous results [33,44]. Fig. 1c and d show GeX monolayer along the zigzag and armchair directions, and the corresponding 2D Brillouin zone (BZ) is shown in Fig. 1b with the high-symmetric points denoted. Similar to phosphorene, this structural anisotropy may also result in the anisotropy of carrier mobility, which will be discussed later in detail.

In order to evaluate the stability of GeX monolayers, we explored the interlayer binding energy (E_B) as a function of interlayer separation d , as illustrated in Fig. 2a and b. The interlayer binding energies are calculated using the formula [45]

$$E_B = (E_{\text{Tot}} - 3E_{\text{Mono}})/2S$$

where E_{Tot} and E_{Mono} are the total energies of GeX trilayer and GeX monolayer, respectively, and S represents the surface area of the GeX trilayer. Considering that a tetragonal cell of GeS and GeSe is used, thus the surface area is determined by the product of the lattice constant (a, b) of the cell. It should be noted that there is no interaction between two layers when E_B becomes to zero, and the smaller the absolute value of E_B , the easier the GeX monolayer could be exfoliated from the multilayer. In light of this definition, the absolute value of E_B can also be considered as the exfoliation energy. At PBE-D2 level of theory, $|E_B|$ are calculated to be 0.52 and

0.45 J m^{-2} for GeS and GeSe monolayers at equilibrium interlayer separation, respectively, which are comparable to the experimentally measured 0.37 J m^{-2} for graphene [46] and significantly lower than that of Ca_2N (1.09 J m^{-2}) [47]. As the interlayer separation increases ($d > 0$) or decreases ($d < 0$), the absolute values of E_B vary in a small range. It is therefore an evidence that GeS and GeSe monolayers can be obtained by mechanical exfoliation from their bulk counterparts.

To clarify the thermal stability of 2D GeS and GeSe monolayers, AIMD simulations were performed. To explore the possible structural rearrangements and decrease in constraint of periodic boundary conditions, we employed 4×4 supercells for the AIMD simulations. The evolution of total energies during AIMD simulations at 500 K is shown in Fig. 2c and d, which demonstrates that 2D GeS and GeSe monolayers are thermally stable at a temperature of 500 K. In addition, snapshots of atomic configurations of 2D GeS and GeSe at the end of AIMD calculations are presented as insets in Fig. 2c and d. It indicates that, after running 3000 steps (3 ps) at the temperature of 500 K, no bond breaking and geometric reconstruction occur, further suggesting the stability of GeX monolayers even at high temperature.

3.2. Mechanical and electronic properties of GeX monolayers

We examined the mechanical properties of 2D GeS and GeSe monolayers. The in-plane elastic stiffness coefficients for 2D structures can be written as follows [48]

$$C_{11} = \frac{1}{A_0} \frac{\partial^2 U}{\partial \varepsilon_{11}^2}, C_{22} = \frac{1}{A_0} \frac{\partial^2 U}{\partial \varepsilon_{22}^2}, C_{12} = \frac{1}{A_0} \frac{\partial^2 U}{\partial \varepsilon_{11} \partial \varepsilon_{22}}$$

Table 1

In-plane elastic stiffness C_{11} , C_{22} and C_{12} of 2D GeS and GeSe. The values of typical 2D materials, MoS₂ and GaSe are listed for reference as well.

Material	C_{11} (Nm^{-1})	C_{22} (Nm^{-1})	C_{12} (Nm^{-1})
GeS	17.6	47.9	24.7
GeSe	13.5	45.6	19.2
MoS ₂ [52]	130	130	32
GaSe [53]	83	83	18

where U is the strain energy in one unit cell and A_0 is the equilibrium unit-cell area of the freestanding GeS and GeSe monolayers. C_{11} and C_{22} characterize the elastic stiffness along x and y directions, respectively. C_{12} can be treated as the coefficient between ε_{11} (uniaxial strain along x direction) and ε_{22} (uniaxial strain along y direction). Since the thickness of GeS and GeSe monolayers is not considered, the unit for the elastic constants is the force per unit length (Nm^{-1}). The in-plane elastic stiffness coefficients of the monolayer can be evaluated by fitting the strain energy U to a series of in-plane strain states ($\varepsilon_{11}, \varepsilon_{22}$), based on the formula

$$U = \frac{1}{2}C_{11}\varepsilon_{11}^2 + \frac{1}{2}C_{22}\varepsilon_{22}^2 + C_{12}\varepsilon_{11}\varepsilon_{22}$$

The atomic positions in the strained unit cell are fully relaxed and the coefficients C_{11} , C_{22} and C_{12} are calculated using a fully relaxed atomic configurations (relaxed-ion stiffness coefficients). **Table 1** summarizes the elastic stiffness coefficients for GeS and GeSe monolayers and the results are in consistent with previous reports [48]. It can be observed that C_{11} is much larger than C_{22} in both GeS and GeSe monolayers, suggesting ε_{22} can be applied more easily in comparison to ε_{11} . In addition, it should be noted that elastic stiffness C_{22} is substantially smaller than that of 2D MoS₂ and

GaSe. This may be attributed to the intrinsic electronic properties of GeX monolayers, where the covalent bonding is weaker than those of 2D MoS₂ [49] and GaSe [50].

The electronic properties of GeX monolayers are calculated by PBE and HSE06 functionals, as shown in Fig. 3a and b of the band structures with red and blue lines representing the PBE and HSE06 results, respectively. At PBE level of theory, we can observe that GeS exhibits an indirect band gap of 1.62 eV while GeSe indicates a direct band gap of 1.10 eV. Specifically, for GeS monolayer, the valence band maximum (VBM) is located on the $\Gamma \rightarrow X$ path, while the conduction band minimum (CBM) lies on the $Y \rightarrow \Gamma$ path, thereby exhibiting an indirect band gap characteristic. Unlike GeS, the direct gap of GeSe monolayer is along the $\Gamma \rightarrow X$ path. Since the PBE functional always underestimates the band gaps of semiconductors, we also examined band structures using the HSE hybrid functional to give band gaps more close to experimental results. HSE06 functional leads to wider band gaps of 2.29 and 1.59 eV for GeS and GeSe monolayers, respectively, without changing the band gap nature (direct or indirect). As indicated in Fig. 3a and b, the CBM or VBM of 2D GeS and GeSe exhibit a strong dispersion, indicating a small effective mass of the carrier m^* for photo-generated carriers. The projected density of states (PDOS) reveal that the electronic states of the valence band near the Fermi level are dominated by S-3p orbitals and partly derive from Ge-4p orbitals, while conduction band close to the Fermi level mainly originates from the Ge-4p orbitals. Therefore, the separation efficiency of the electrons and holes could be affected by the spatial charge distribution of CBM and VBM [51]. We also explored the partial charge densities of the CBM and VBM of 2D GeX monolayers, as shown as insets in Fig. 3a and b. It can be obviously seen that the VBM are mainly composed of p orbitals of S/Se atoms, while the CBM are predominantly con-

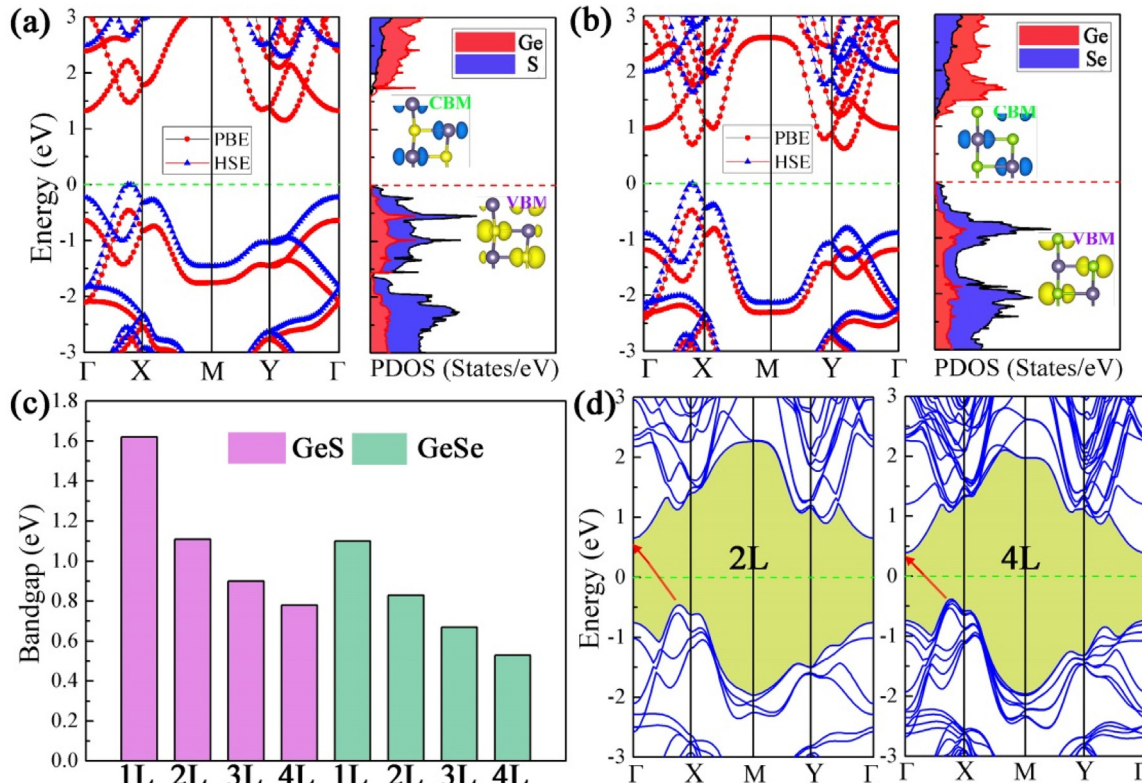


Fig. 3. Band structures and projected density of states (PDOS) of (a) GeS and (b) GeSe monolayers. The red and blue lines represent the PBE and HSE06 results, respectively. Simultaneously, the CBM and VBM of GeS and GeSe monolayers are presented as insets in the PDOS plot, where the value of isosurface is set to be $0.012e/\text{\AA}^3$. (c) Band gaps of GeS and GeSe as the dependence of layer number by PBE calculations. (d) Band structures of GeS bilayer and four-layer. The Fermi level is set to 0 eV. (For interpretation of the references to colour in this figure legend, the reader is referred to the web version of this article.)

tributed by the p orbitals of Ge atoms. These results are in good agreement with the results of PDOS in Fig. 3a and b. Similar to the distribution of VBM and CBM within the type-II heterostructures, the photo-generated electrons and holes would transfer to CBM (Ge) and VBM (S/Se), respectively, and thus is beneficial for the separation of excited electrons and holes. In addition, the variation of the band gap with thickness from one-layer (1L) to four-layers (4L) is evaluated for 2D GeS and GeSe, as shown in Fig. 3c. The multi-layer GeX along the c -axis shows AA stacking order with Ge atom just above the Ge atom of the other layer. It can be observed that the band gaps of both GeS and GeSe monolayers undergo a significant decrease when the number of layer changes from one to two, and then the values change slightly for thicker layers. In addition, as shown in Fig. 3d, GeS monolayer would maintain the indirect gap character as the layer number increases. Specifically, the position of CBM moves from a point along $Y \rightarrow \Gamma$ to the Γ point, while the VBM still locates at a point along $\Gamma \rightarrow X$. Such an interesting phenomenon demonstrates an opportunity for tuning the electronic properties of GeS by thickness control.

3.3. Migration and separation of photo-generated electron-hole pairs

For efficient photocatalytic solar water splitting, materials with visible-light harvesting ability and electrons and/or holes with high mobilities for promoting charge separation are required. Herein, we explored the carrier mobility μ of 2D GeS and GeSe. In a 2D semiconductor, the carrier mobility is mainly dominated by the phonon scattering, which can be described by the deformation potential (DP) theory [52]. Therefore, based on the DP theory, the carrier

mobility can be determined by the following analytical expression [53]

$$\mu = \frac{2e\hbar^3 C}{3K_B T |m^*|^2 E_d^2}$$

where e , \hbar , K_B and T represent the electron charge, reduced Planck constant, Boltzmann constant and temperature, respectively. And C is the elastic modulus caused by uniaxial strain along specific directions, which is given by $C = (\partial^2 E / \partial \epsilon^2) / S_0$, with E being the total energy under uniaxial strain and S_0 being the area of the system. The uniaxial strain is defined as $\epsilon = \Delta a / a_0$, where a_0 is the lattice constants of the freestanding monolayer. Besides, m^* is the effective mass of the carrier, which is defined as $m^* = \hbar^2 (\partial^2 E(k) / \partial k^2)^{-1}$. E_d is the deformation potential constant of the carrier, calculated by using $E_d = \partial E_{\text{edge}} / \partial \epsilon$. E_{edge} is the energy level of holes in the VBM and electrons in the CBM.

The carrier mobility of 2D GeS and GeSe was investigated along x and y directions, as illustrated in Fig. 4a. To obtain the elastic modulus C and deformation potential constant E_d , we computed the total energy and band edge positions as a function of the uniaxial strain along x and y directions and the results are shown in Fig. 4b and c. It is shown that our results satisfy not only the parabolic fitting of total energies, but also the linear fittings of CBM and VBM positions. All of the calculated values of m^* , C , E_d and μ are summarized in Table 2. It can be observed that the calculated carrier mobility for 2D GeS and GeSe shows an anisotropic character with the values ranging from several tens to a few thousands $\text{cm}^2 \text{V}^{-1} \text{s}^{-1}$. Specifically, for 2D GeS monolayer, the electrons mobility along the x direction is $2430.50 \text{ cm}^2 \text{V}^{-1} \text{s}^{-1}$, while the mobility of holes

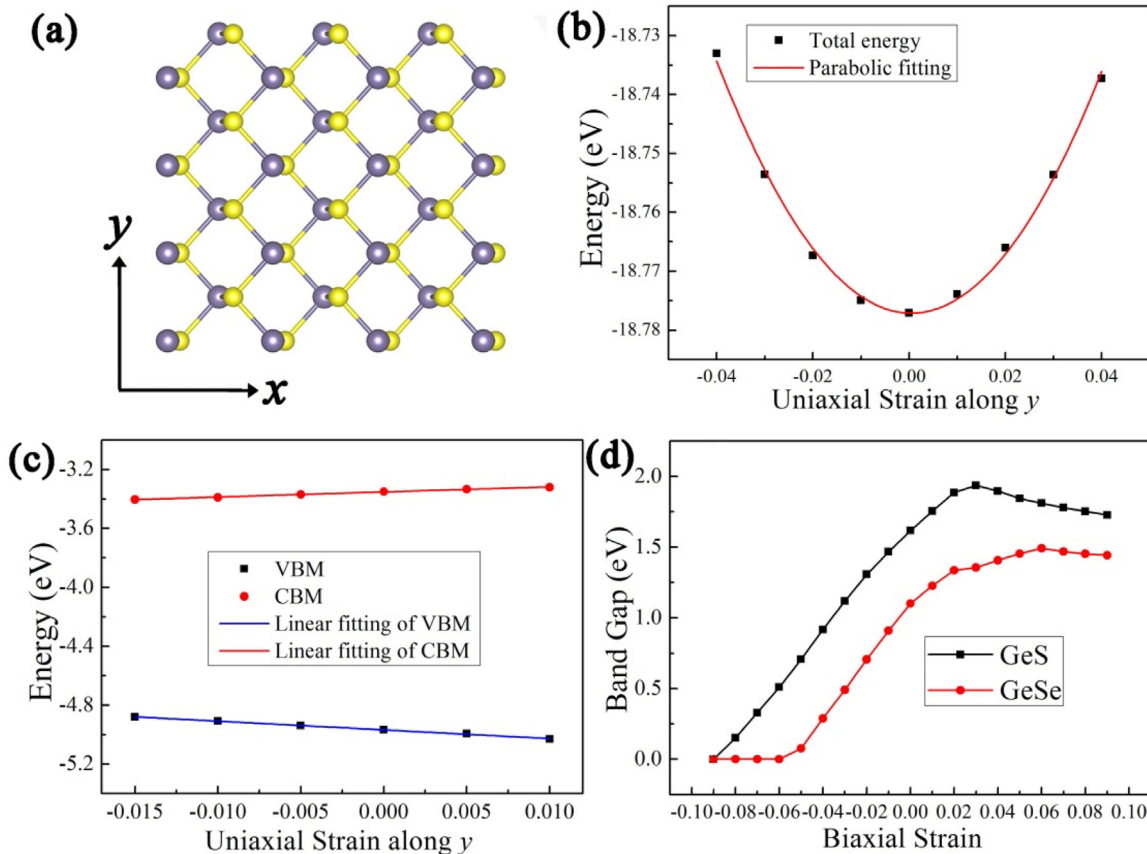


Fig. 4. (a) Top view of the atomic structure of GeX monolayers with x and y directions defined. (b) The energy and (c) the band edge (CBM and VBM) positions of 2D GeS as a function of the uniaxial strain. (d) Band gap of GeX monolayers as a function of biaxial strain.

Table 2

At the PBE level of theory, the carrier effective masses (m^*), elastic modulus (C), deformation potential constant (E_d), and carrier mobility (μ) of the investigated GeX monolayer.

2D materials	Carrier type	m^*/m_0	C (Nm ⁻¹)	E_d (eV)	μ (cm ² V ⁻¹ s ⁻¹)
GeS	Electrons (x)	0.22	16.26	1.40	2430.50
	Holes (x)	0.23	16.26	6.13	115.99
	Electrons (y)	0.44	52.37	3.46	320.09
	Holes (y)	0.59	52.37	5.93	60.67
GeSe	Electrons (x)	0.14	15.92	1.69	4032.64
	Holes (x)	0.15	15.92	5.57	323.42
	Electrons (y)	0.25	51.84	2.75	1555.23
	Holes (y)	0.31	51.84	10.01	76.33

at the VBM is about 115.99 cm²V⁻¹s⁻¹ in x direction. Therefore, the mobility of electrons in x direction is more than twenty times larger than the holes, which can be interpreted by the significantly larger effective masses of holes than electrons. While for the case in y direction, the mobility of electrons is more than five times larger than the holes. Likewise, the similar results were obtained for 2D GeSe monolayer. Remarkably, the electron mobility in x direction could reach 4032.64 cm²V⁻¹s⁻¹, which could be comparable to or even higher than that of many other 2D materials, such as MnPSe₃ (625.9 cm²V⁻¹s⁻¹) [23], MoS₂ (200 cm²V⁻¹s⁻¹) [54] and BN (487 cm²V⁻¹s⁻¹) [55]. On one hand, the outstanding carrier mobility would lead to fast migration of photo-generated electrons and holes, which can render the carriers quickly migrate to the surface of the semiconductor to participate in the redox reaction. On the other hand, the significant difference between electron mobility and hole mobility could further reduce the probability of the recombination of photo-generated carriers, significantly improving the photocatalytic activity of 2D GeS and GeSe.

For an efficient photocatalyst, high photo-generated carrier separation efficiency is advantageous for improving the photocatalytic activity. Here, the exciton binding energy (E_{eb}) is calculated to explore the carrier separation efficiency. The dielectric constants are obtained by density functional perturbation theory (DFPT) using the linear response method. The macroscopic static dielectric tensor (ε) can be defined as the sum of electronic (ε_{ion}) and ionic (ε_{ele}) contributions. Using the hydrogenic model, the exciton binding energy and exciton Bohr radius (a^*) can be estimated as follows [56]

$$E_{eb} = \frac{\mu}{m_0 \varepsilon^2} R_H a^* = \frac{m_0}{\mu} \varepsilon a_H$$

where R_H , m_0 and μ are the Rydberg constant of the hydrogen atom (13.6 eV), the free electron mass and the effective reduced mass, respectively. a_H is the Bohr radius of the hydrogen atom. It should be noted that the 2D dielectric screening is different from the three-dimensional (3D) one [57], so the hydrogenic model is probably just a convenient approximation. The calculated static dielectric constant, exciton binding energy and exciton Bohr radius for GeS and GeSe are given in Table 3. For GeS monolayer, it is noted that the exciton binding energy and Bohr radius are estimated to be 109 meV and 14 Å, respectively. Likewise, for GeS monolayer, the calculated exciton binding energy and Bohr radius are 12 meV and 57 Å, respectively. Besides, we also calculate the exciton binding

energy of other typical 2D materials (MoS₂ and C₃N₄) for comparison. The exciton binding energy is explored to be 280 and 728 meV for MoS₂ and C₃N₄, respectively. The apparently low exciton binding energy of GeS and GeSe indicates that the exciton can be easily dissociated into free charge carriers. In view of the high carrier separation efficiency, our results show that 2D GeS and GeSe monolayers can be promising photocatalytic materials because of the high static dielectric constant and low exciton binding energy.

In recent years, many studies have demonstrated that the external strain has a rather pronounced effect on the electronic properties of 2D materials [44]. In order to gain an insight into the response of the electronic properties of 2D GeS and GeSe to mechanical strain (compressive and tensile strain), we apply small biaxial strain ($-10\% \leq \epsilon \leq 10\%$) on the 2D GeS and GeSe monolayers. As shown in Fig. 4d, band gaps of 2D GeS and GeSe exhibit a linear decrease under compressive strain, and then becomes zero when compressive strain is up to -10% (for GeS) and -6% (for GeSe), demonstrating a semiconductor-metal transition in GeS and GeSe monolayers. In addition, in contrast to the compressive strain, the effect of the tensile strain is more complicated. The band gaps of 2D GeS and GeSe firstly increase as the tensile strain increases. When the tensile strain is larger than 4%, the band gaps begin to decrease with the increase of tensile strain. Fig. 5 shows the band structures of GeS and GeSe monolayers under different biaxial strain. Interestingly, the VBM of GeS monolayer moves to the Γ point at a tensile strain of 4%. Upon the application of strain, the band structures can be modulated and an indirect-direct band gap transition is observed in GeS monolayer. The above results suggest that the band structures of GeS and GeSe monolayers can be flexibly modulated by applying an external strain, providing an efficient route to tune the electronic properties of 2D GeS and GeSe and expand the scope of application.

3.4. Band alignment of single- and few-layer GeS and GeSe with water redox potentials

For efficient photocatalyst in practice, there are several criteria that 2D GeS and GeSe should fulfill. Primarily, the band gap should be larger than 1.23 eV and smaller than 3 eV to enhance solar light absorption. In addition, the band edges must straddle the water redox potentials. Specifically, the CBM should be higher than the reduction potential of H⁺/H₂ (-4.44 eV) and the VBM should be lower than the oxidation potential of O₂/H₂O (-5.67 eV). As the appropriate band gaps have been obtained, we also need to examine the band edges with respect to the water redox potentials. As depicted in Fig. 6, it is observed that the band edges of 2D GeS and GeSe cannot straddle the water redox potential since the VBM is higher than the oxidation potential of O₂/H₂O. Nevertheless, considering that the electronic structures can be tuned, tensile strain is applied to modify the positions of band edges to satisfy the water redox potentials. As expected, the band alignments of 2D GeS and GeSe could straddle the water redox potentials as the tensile strain

Table 3

Calculated static dielectric constant, exciton binding energy (E_{eb}) and exciton Bohr radius (a^*) for GeS and GeSe monolayers.

	ε_{ion}			ε_{ele}			E_{eb} (meV)	a^* (Å)
	x	y	z	x	y	z		
GeS	1.81	3.05	0.01	3.78	3.75	1.32	109	14
GeSe	3.26	8.09	0.01	6.06	6.38	1.33	12	57

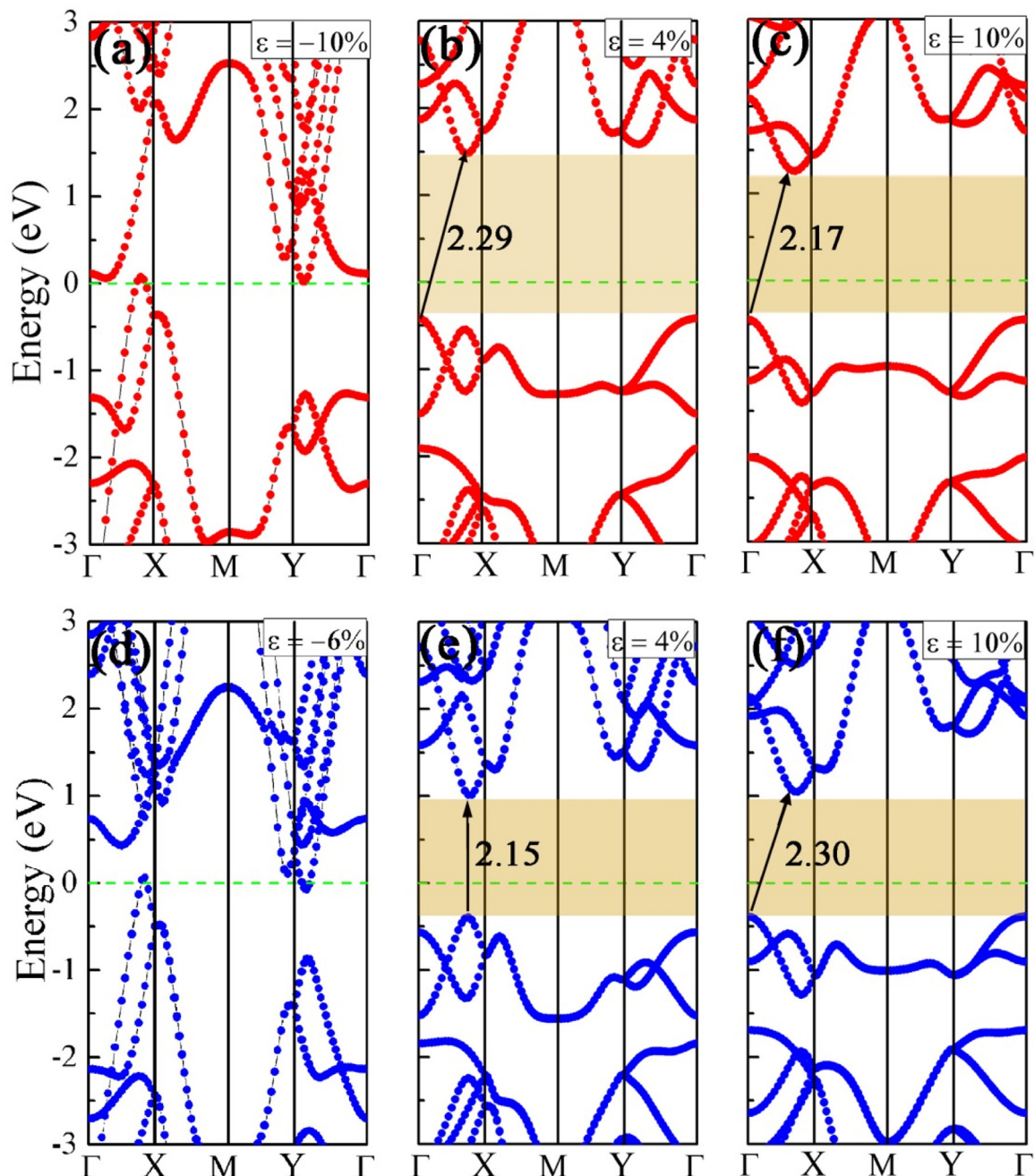


Fig. 5. At PBE level of theory, band structures of GeS monolayer under (a) -10%, (b) 4% and (c) 10% biaxial strain. And band structures of GeSe monolayer under (d) -6%, (e) 4% and (f) 10% biaxial strain. The Fermi level is set to 0 eV.

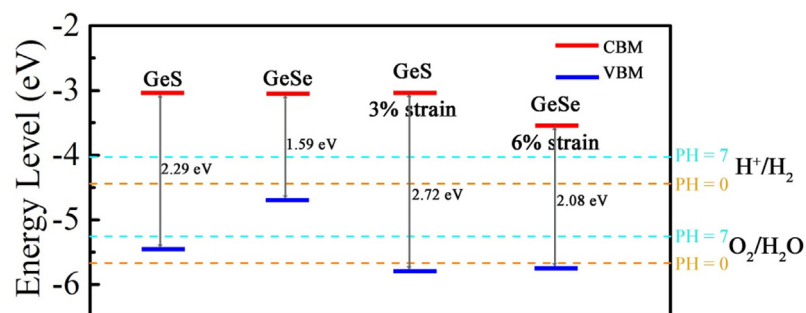


Fig. 6. Band edge position of VBM and CBM with respect to water redox potential calculated by HSE06 functional of 2D freestanding GeS and GeSe under different tensile strain. The orange and cyan dashed lines represent the redox potential of water splitting at pH = 0 and pH = 7, respectively. (For interpretation of the references to colour in this figure legend, the reader is referred to the web version of this article.)

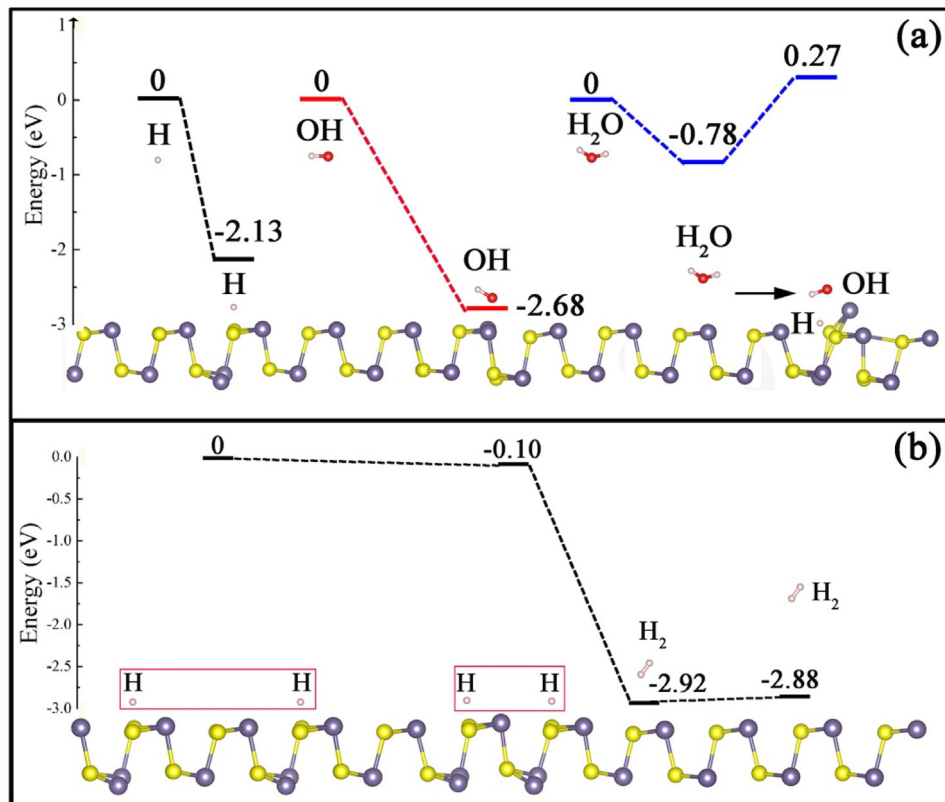


Fig. 7. (a) Adsorption configurations of H, OH, and H₂O, and decomposition mechanism of H₂O on 2D GeS. (b) Interaction between two hydrogen adatoms, formation and releasing of hydrogen molecules on/from 2D GeS. The red balls represent the oxygen atoms and the gray balls represent hydrogen atoms. (For interpretation of the references to colour in this figure legend, the reader is referred to the web version of this article.)

is up to 3% and 6%, respectively. In addition, it should be noted that the water redox potential depends on the pH value [58]. The standard oxidation potential O₂/H₂O in a solution can be calculated by $E_{O_2/H_2O}^{ox} = -5.67\text{eV} + \text{pH} \times 0.059\text{eV}$ and the reduction potential for H⁺/H₂ is determined by $E_{H^+/H_2}^{red} = -4.44\text{eV} + \text{pH} \times 0.059\text{eV}$. It should be noted that the unique feature of chalcogenides is the high stability in an acidic environment, especially if in combination with other transition metals [59]. In spite of that, some sulfides and selenides might be unstable in an acidic environment [23]. For example, metal chalcogenides (Mo_xRu_ySe_z, Ru_xX_y (where X=S, Se, and Te)) are actually unstable in acidic and oxidizing atmosphere [60]. CdS and CdSe are also unstable in acidic media and can be corroded easily [61]. Thus, the redox potential at neutral environment (pH = 7) was also computed. Except the freestanding 2D GeSe without strain, as shown in Fig. 6, the band edges of the other three cases straddle the water redox potentials at pH = 7. Moreover, the CBM positions of these materials are high enough with respect to the reduction potential of H⁺/H₂, indicating that the driving force for the water reduction reaction is strong. Besides, we also examined the band alignment of few-layer (from two- to four-layer) GeS and GeSe. The results indicate that the position of CBM of few-layer GeS and GeSe locates more negative than the redox potential of H⁺/H₂ (0 V vs NHE), but the VBM is not more positive than the redox potential of O₂/H₂O (1.23 V vs NHE). Therefore, the band edges of few-layer GeS and GeSe do not straddle the water redox potentials, and they can only be used for the water oxidation or reduction process in Z-scheme photocatalysis.

3.5. Water adsorption and decomposition on the surface of 2D GeS

To further reveal the mechanism of photocatalytic hydrogen formation on 2D GeX, we simulated the redox reactions of water on GeX monolayers. Considering that 2D GeS and GeSe share the same geometric configuration, here we only employed 2D GeS as the model system. Since the formation of hydrogen molecules starts from the decomposition of adsorbed water, we first investigated the adsorption behavior of H, OH and H₂O on 2D GeS, and the corresponding adsorption energies are -2.13, -2.68 and -0.78 eV, respectively, as shown in Fig. 7a. Negative values indicate that the adsorption of H, OH and H₂O on 2D GeS is energetically favorable. In addition, it should be noted that the subsequent water decomposition on 2D GeS is an endothermic reaction with a reaction energy of 1.05 eV (from -0.78 to 0.27 eV), which is similar to the water decomposition reaction on TiO₂ surfaces [62]. Furthermore, as the generated hydrogen atoms are adsorbed on 2D GeS, the remotely separated hydrogen adatom will be energetically favorable to migrate close to form hydrogen molecules. As displayed in Fig. 7b, the reaction energy required for removing one H₂ from 2D GeS is relatively small (0.04 eV). From the viewpoint of energy, this indicates that the adsorbed H₂ is easy to be released, which is beneficial for photocatalytic hydrogen gas production. Meanwhile, similar to 2D Zr₂CO₂ [63].

The high specific surface area of 2D GeS and GeSe are beneficial for the photocatalytic reactions, and this will further enhance the efficiency of photocatalytic water splitting.

4. Conclusion

In conclusion, we theoretically explored the structural and electronic properties of 2D GeS and GeSe monolayers based on the first-principles calculations and deformation potential theory. The thermal stabilities of 2D GeX monolayers are proved by AIMD simulations, suggesting that 2D GeX are feasible even at 500 K. Remarkably, we found that both GeS and GeSe monolayers present not only suitable band gaps (1.59 and 2.29 eV), but also proper band edge positions under biaxial strain at neutral environment. Combining the effective migration and separation of carriers, 2D GeS and GeSe monolayers have a great possibility to be used as photocatalysts for overall water splitting. Our study highlights 2D GeX monolayers in the application as photocatalysts and provides useful guidance for further expanding the practical application range of 2D GeX materials.

Acknowledgements

This work is supported by the National Basic Research Program of China (973 program, under Grant No. 2013CB632401), the National Natural Science foundation of China (under Grant No. 21333006, 11404187 and 11374190), the Taishan Scholar Program of Shandong Province, 111 Project B13029.

References

- [1] H.B. Gray, Powering the planet with solar fuel, *Nat. Chem.* 1 (2009) 7.
- [2] W. Lubita, Hydrogen: an overview, *B. Tumas, Chem. Rev.* 107 (2007) 3900–3903.
- [3] A.J. Esswein, D.G. Nocera, Hydrogen production by molecular photocatalysis, *Chem. Rev.* 107 (2007) 4022–4047.
- [4] B. Chen, S.H. Shen, L.J. Guo, S.S. Mao, Semiconductor-based photocatalytic hydrogen generation, *Chem. Rev.* 110 (2010) 6503–6570.
- [5] J. Lin, Y. Liu, N.Y. Liu, Y.Z. Han, X. Zhang, H. Huang, Y. Lifshitz, S.T. Lee, J. Zhong, Z.H. Kang, Metal-free efficient photocatalyst for stable visible water splitting via a two-electron pathway, *Science* 347 (2015) 970–974.
- [6] Q.J. Xiang, J.G. Yu, M. Jaroniec, Graphene-based semiconductor photocatalysts, *Chem. Soc. Rev.* 41 (2012) 782–796.
- [7] K. Maeda, K. Domen, Photocatalytic water splitting: recent progress and future challenges, *J. Phys. Chem. Lett.* 1 (2010) 2655–2661.
- [8] P.W. Du, R. Eisenberg, Catalysts made of earth-abundant elements (Co, Ni, Fe) for water splitting: recent progress and future challenges, *Energy Environ. Sci.* 5 (2012) 6012–6021.
- [9] W.Y. Choi, A. Termin, M.R. Hoffmann, The role of metal ion dopants in quantum-sized TiO₂ correlation between photoreactivity and charge carrier recombination dynamics, *J. Phys. Chem.* 98 (1994) 13669–13679.
- [10] R. Asahi, T. Morikawa, T. Ohwaki, K. Aoki, Y. Taga, Visible-light photocatalysis in nitrogen-doped titanium oxides, *Science* 293 (2001) 269–271.
- [11] U. Diebold, The surface science of titanium dioxide, *Surf. Sci. Rep.* 48 (2003) 53–229.
- [12] S.B. Wang, Z.X. Ding, X.C. Wang, A stable ZnCo₂O₄ cocatalyst for photocatalytic CO₂ reduction, *Chem. Commun.* 51 (2015) 1517–1519.
- [13] S.B. Wang, Y.D. Hou, X.C. Wang, Development of a stable MnCo₂O₄ cocatalyst for photocatalytic CO₂ reduction with visible light, *ACS Appl. Mater. Interfaces* 7 (2015) 4327–4335.
- [14] D.M. Chen, K.W. Wang, W.Z. Hong, R.L. Zong, W.Q. Yao, Y.F. Zhu, Visible light photoactivity enhancement via CuTCPP hybridized g-C₃N₄ nanocomposite, *Appl. Catal. B: Environ.* 166–167 (2015) 366–373.
- [15] A. Fujishima, H. Honda, Electrochemical photolysis of water at a semiconductor electrode, *Nature* 238 (1972) 37–38.
- [16] S.B. Wang, W.S. Yao, J.L. Lin, Z.X. Ding, X.C. Wang, Cobalt imidazolate metal-organic frameworks photosensitize CO₂ under mild reaction conditions, *Angew. Chem. Int. Ed.* 53 (2014) 1034–1038.
- [17] S.B. Wang, J.L. Lin, X.C. Wang, Semiconductor-redox catalysis promoted by metal-organic frameworks for CO₂ reduction, *Phys. Chem. Chem. Phys.* 16 (2014) 14656–14660.
- [18] M. Zhang, W.J. Jiang, D. Liu, J. Wang, Y.F. Liu, Y.Y. Zhu, Y.F. Zhu, Photodegradation of phenol via C₃N₄-agar hybrid hydrogel 3D photocatalysts with free separation, *Appl. Catal. B: Environ.* 183 (2016) 263–268.
- [19] K.S. Novoselov, A.K. Geim, S.V. Morozov, D. Jiang, Y. Zhang, S.V. Dubonos, I.V. Grigorieva, A.A. Firsov, Electric field effect in atomically thin carbon films, *Science* 306 (2004) 666–669.
- [20] W. Wei, T. Jacob, Strong many-body effects in silicone-based structures, *Phys. Rev. B* 88 (2013) 045203.
- [21] Y.D. Ma, Y. Dai, Y.B. Lu, B.B. Huang, Effective bandgap engineering in wrinkled germanane via tiny electric field, *J. Mater. Chem. C* 2 (2014) 1125–1130.
- [22] S. Garaj, W. Hubbard, A. Reina, J. Kong, D. Branton, J.A. Golovchenko, Graphene as a subnanometre trans-electrode membrane, *Nature* 467 (2010) 190–193.
- [23] X. Zhang, X.D. Zhao, D.H. Wu, Y. Jing, Z. Zhou, MnPS₃ monolayer: a promising 2D visible-light photohydrolytic catalyst with high carrier mobility, *Adv. Sci. 3* (2016) 1600062.
- [24] R. Li, Y. Dai, M.M. Li, B.B. Huang, Stable Si-based pentagonal monolayers: high carrier mobilities and applications in photocatalytic water splitting, *J. Mater. Chem. A* 3 (2015) 24055–24063.
- [25] Y.F. Sun, Z.H. Sun, S. Gao, H. Cheng, Q.H. Liu, J.Y. Piao, T. Yao, C.Z. Wu, S.L. Hu, S.Q. Wei, Y. Xie, Fabrication of flexible and freestanding zinc chalcogenide single layers, *Nat. Commun.* 3 (2012) 1057.
- [26] J. Zhu, T.M. Zhang, Z.J. Sun, H.L. Chen, J. Guan, X. Chen, H.X. Ji, P.W. Du, S.F. Yang, Black phosphorus revisited: a missing metal-free elemental photocatalyst for visible light hydrogen evolution, *Adv. Mater.* (2017) 1605776.
- [27] S.M. Yoon, H.J. Song, H.C. Choi, P-type semiconducting GeSe combs by a vaporization-condensation-recrystallization (VCR) process, *Adv. Mater.* 22 (2010) 2164–2167.
- [28] A.S. Rodin, L.C. Gomes, A. Carvalho, A.H. Neto, Valley physics in tin (II) sulfide, *Phys. Rev. B* 93 (2016) 045431.
- [29] L.C. Gomes, A. Carvalho, Phosphorene analogues: isoelectronic two-dimensional group-IV monochalcogenides with orthorhombic structure, *Phys. Rev. B* 92 (2015) 085406.
- [30] L. Li, Z. Chen, Y. Hu, X. Wang, T. Zhang, W. Chen, Q. Wang, Single-layer single-crystalline SnSe nanosheets, *J. Am. Chem. Soc.* 135 (2013) 1213–1216.
- [31] P. Ramasamy, D. Kwak, D.H. Lim, H.S. Ra, J.S. Lee, Solution synthesis of GeS and GeSe nanosheets for high-sensitivity photodetectors, *J. Mater. Chem. C* 4 (2016) 479–485.
- [32] G. Shi, E. Kioupakis, Anisotropic spin transport and strong visible-light absorbance in fer-layer SnSe and GeSe, *Nano Lett.* 15 (2015) 6926–6931.
- [33] F. Li, X. Liu, Y. Wang, Y. Li, Germanium monosulfide monolayer: a novel two-dimensional semiconductor with a high carrier mobility, *J. Mater. Chem. C* 4 (2016) 2155–2159.
- [34] G. Kresse, J. Furthmüller, Efficiency of ab-initio total energy calculations for metals and semiconductors using a plane-wave basis set, *Comput. Mater. Sci.* 6 (1996) 15–50.
- [35] G. Kresse, Efficient iterative schemes for ab initio total-energy calculations using a plane-wave basis set, *Phys. Rev. B* 54 (1996) 11169–11186.
- [36] P.E. Blochl, Projector augmented-wave method, *Phys. Rev. B* 50 (1994) 17953–17979.
- [37] J.P. Perdew, Accurate and simple analytic representation of the electron-gas correlation energy Y. Wang, *Phys. Rev. B* 45 (1992) 13244–13249.
- [38] J.P. Perdew, K. Burke, M. Ernzerhof, Generalized gradient approximation made simple, *Phys. Rev. Lett.* 77 (1996) 3865–3968.
- [39] H.J. Monkhorst, J.D. Pack, Special points for Brillouin-zone integrations, *Phys. Rev. B* 13 (1976) 5188–5192.
- [40] A. Tkatchenko, M. Scheffler, Accurate molecular van der Waals interactions from ground-state electron density and free-atom reference data, *Phys. Rev. Lett.* 102 (2009) 073005.
- [41] J.P. Perdew, Density functional theory and the band gap problem, *Int. J. Quantum Chem.* 19 (1986) 497–523.
- [42] J. Heyd, G.E. Scuseria, M. Ernzerhof, Hybrid functionals based on a screened coulomb potential, *J. Chem. Phys.* 118 (2003) 8207–8215.
- [43] H.J. Zhang, D.H. Wu, Q. Tang, L. Liu, Z. Zhou, ZnO/GaN heterostructured nanosheets for solar energy harvesting: computational studies based on hybrid density functional theory, *J. Mater. Chem. A* 1 (2013) 2231–2237.
- [44] W.Y. Yu, Z.L. Zhu, S.L. Zhang, X.L. Cai, X.F. Wang, C.Y. Niu, W.B. Zhang, Tunable electronic properties of GeSe/phosphorene heterostructure from first-principles study, *Appl. Phys. Lett.* 109 (2016) 103104.
- [45] C. Xin, J.X. Zheng, Y.T. Su, S.K. Li, B.K. Zhang, Y.C. Feng, F. Pan, Few-layer tin sulfide: a new black-phosphorus-analogue 2D material with a sizeable band gap odd-even quantum confinement effect, and high carrier mobility, *J. Phys. Chem. C* 120 (2016) 22663–22669.
- [46] R. Zacharia, H. Ulbricht, T. Hertel, Interlayer cohesive energy of graphite from thermal desorption of polyaromatic hydrocarbons, *Phys. Rev. B* 69 (2004) 155406.
- [47] S. Zhao, Z. Li, J. Yang, Obtaining two-dimensional electron gas in free space without resorting to electron doping: an electron based design, *J. Am. Chem. Soc.* 136 (2014) 13313–13318.
- [48] R.X. Fei, W.B. Li, J. Lu, L. Yang, Giant piezoelectricity of monolayer group IV monochalcogenides: snSe SnS, GeSe, and GeS, *Appl. Phys. Lett.* 107 (2015) 173104.
- [49] K.A.N. Duerloo, M.T. Ong, E.J. Reed, Intrinsic piezoelectricity in two-dimensional materials, *J. Phys. Chem. Lett.* 3 (2012) 2871–2876.
- [50] W.B. Li, J. Li, Piezoelectricity in two-dimensional group-II monochalcogenides, *Nano Res.* 8 (2015) 3796–3802.
- [51] H.J. Zhang, G. Yang, X.Q. Zuo, H.B. Tang, Q. Yang, G. Li, Computational studies on the structural, electronic and optical properties of graphene-like MXenes (M₂CT₂ M = Ti, Zr, Hf; TO, F, OH) and their potential applications as visible-light driven photocatalysts, *J. Mater. Chem. A* 4 (2016) 12913–12920.
- [52] J. Barden, W. Shockley, Deformation potentials and mobilities in non-polar crystals, *Phys. Rev.* 80 (1950) 72–80.
- [53] J. Dai, X.C. Zeng, Titanium trisulfide monolayer: theoretical prediction of a new direct-gap semiconductor with high and anisotropic carrier mobility, *Angew. Chem. Int. Ed.* 54 (2015) 7572–7576.

- [54] B. Radisavljevic, A. Radenovic, J. Brivio, V. Giacometti, A. Kis, Single-layer MoS₂ transistors, *Nat. Nanotechnol.* 6 (2011) 147–150.
- [55] S. Bruzzone, G. Fiori, Ab-initio simulations of deformation potentials and electron mobility in chemically modified graphene and two-dimensional hexagonal boron-nitride, *Appl. Phys. Lett.* 99 (2011) 222108.
- [56] M. Dvorak, S.H. Wei, Z.G. Wu, Origin of the variation of exciton binding energy in semiconductors, *Phys. Rev. Lett.* 110 (2013) 016402.
- [57] P. Cudazzo, I.V. Tokatly, A. Rubio, Dielectric screening in two-dimensional insulators: implications for excitonic and impurity states in graphene, *Phys. Rev. B* 84 (2011) 085406.
- [58] H.L. Zhuang, R.G. Hennig, Single-layer group-II monochalcogenides photocatalysts for water splitting, *Chem. Mater.* 25 (2013) 3232–3238.
- [59] N.A. Vante, W. Jaegermann, H. Tributsch, W. Honle, K. Yvon, Electrocatalysis of oxygen reduction by chalcogenides containing mixed transition metal clusters, *J. Am. Chem. Soc.* 109 (1987) 3251–3257.
- [60] Y. Ohgi, A. Ishihara, K. Matsuzawa, S. Mitsushima, K.-I. Ota, M. Matsumoto, H. Imai, Factors for improvements of catalytic activity of zirconium oxide-based oxygen-reduction electrocatalysts, *J. Electrochem. Soc.* 160 (2013) 162–167.
- [61] A. Nemcsics, S. Kovacs, Z. Labadi, K.-F. Hesse, M. Czank, P. Turmezei, S. Motrya, Novel material for an electrochemical solar cell, *Sol. Energ. Mat. Sol. C* 89 (2005) 175–183.
- [62] Z.Y. Zhao, Z.S. Li, Z.G. Zou, A theoretical study of water adsorption and decomposition on the low-index stoichiometric anatase TiO₂ surfaces, *J. Phys. Chem. C* 116 (2012) 7430–7441.
- [63] Z.L. Guo, J. Zhou, L.C. Zhu, Z.M. Sun, MXene: a promising photocatalyst for water splitting, *J. Mater. Chem. A* 4 (2016) 11446–11452.